Biophysical Journal Volume 108 March 2015 1187–1198



Article

# Probing the Huntingtin 1-17 Membrane Anchor on a Phospholipid Bilayer by Using All-Atom Simulations

Sébastien Côté,[1,*] Vincent Binette,[1] Evgeniy S. Salnikov,[2] Burkhard Bechinger,[2] and Normand Mousseau[1,*]

[1]Département de Physique and Groupe de Recherche sur les Protéines Membranaires, Université de Montréal, Montréal, Québec, Canada; and [2]Université de Strasbourg/Centre National de la Recherche Scientifique, UMR7177, Institut de Chimie, Strasbourg, France

ABSTRACT Mislocalization and aggregation of the huntingtin protein are related to Huntington's disease. Its first exon—more specifically the first 17 amino acids (Htt17)—is crucial for the physiological and pathological functions of huntingtin. It regulates huntingtin's activity through posttranslational modifications and serves as an anchor to membrane-containing organelles of the cell. Recently, structure and orientation of the Htt17 membrane anchor were determined using a combined solution and solid-state NMR approach. This prompted us to refine this model by investigating the dynamics and thermodynamics of this membrane anchor on a POPC bilayer using all-atom, explicit solvent molecular dynamics and Hamiltonian replica exchange. Our simulations are combined with various experimental measurements to generate a high-resolution atomistic model for the huntingtin Htt17 membrane anchor on a POPC bilayer. More precisely, we observe that the single $\alpha$-helix structure is more stable in the phospholipid membrane than the NMR model obtained in the presence of dodecylphosphocholine detergent micelles. The resulting Htt17 monomer has its hydrophobic plane oriented parallel to the bilayer surface. Our results further unveil the key residues interacting with the membrane in terms of hydrogen bonds, salt-bridges, and nonpolar contributions. We also observe that Htt17 equilibrates at a well-defined insertion depth and that it perturbs the physical properties—order parameter, thickness, and area per lipid—of the bilayer in a manner that could favor its dimerization. Overall, our observations reinforce and refine the NMR measurements on the Htt17 membrane anchor segment of huntingtin that is of fundamental importance to its biological functions.

## INTRODUCTION

Huntingtin is an ubiquitous protein of 3114 amino acids fundamental to the embryonic development (1) and is involved, for example, in intracellular vesicular and organelles trafficking (2) such as regulating autophagy in response to endoplasmic reticulum stress (3), protein scaffolding (4), and transcription and axonal transport (5). It has attracted considerable attention over the last few decades due to its relation to Huntington's disease, a CAG/glutamine repeat disorder (6–9). Indeed, it contains a segment of consecutive glutamines ($Q_N$) at its amino-terminus that, when expressed with >~36 repeating residues, leads to the aggregation of huntingtin, in a dominant manner, causing deleterious effects through various nuclear and extranuclear pathways (10,11). It has been observed that amino-terminus fragments generated by proteolytic cleavage of huntingtin accumulate in the nucleus and are involved in the pathogenesis of Huntington's disease (12–14). The first exon of huntingtin is sufficient to reproduce neurological phenotypes and aggregation features characteristic of Huntington's disease in vivo (15,16) and in vitro (17–19). It is composed of three main regions: an amphipathic segment of 17 amino acids (Htt17), a segment of consecutive glutamines ($Q_N$), and a segment rich in prolines.

The Htt17 segment of the first exon is of fundamental importance. It acts as a membrane anchor that modulates the localization of huntingtin to specific membrane-containing organelles of the cell such as the endoplasmic reticulum (20), the mitochondria, and the Golgi (21). Htt17 also acts as a nuclear export sequence that regulates the localization of huntingtin between the cytoplasm and the nucleus (22,23). It interacts with the TRiC chaperonin to suppress the aggregation of huntingtin (24). And it can undergo posttranslational modifications such as SUMOylation (25) and phosphorylation (26–29) that modulate the toxicity, clearance, localization, and function of huntingtin. This small segment also accelerates the fibrillation kinetics (24,30) and changes the nucleation and the oligomer structures (31,32) of the amyloidogenic $Q_N$ segment (33). These observations indicate that Htt17 is crucial to huntingtin physiological and pathological functions.

In aqueous solution, circular dichroism (CD) experiments show that the Htt17 segment populates 10–50% of $\alpha$-helix depending on the aqueous buffer used (20,24,34,35). Solution nuclear magnetic resonance (NMR) studies further indicate that it does not sample any stable secondary structure motif (24). Taken together, these results suggest that Htt17 likely populates a wide range of helix/coil

*Submitted October 3, 2014, and accepted for publication February 2, 2015.*

*Correspondence: sebastien.cote.4@umontreal.ca or normand.mousseau@umontreal.ca

Editor: Michael Feig.



0006-3495/15/03/1187/12 $2.00

http://dx.doi.org/10.1016/j.bpj.2015.02.001

configurations. In contrast, Htt17 appears to form an $\alpha$-helix in a crystal structure of a fusion protein consisting of the maltose-binding protein and huntingtin exon 1 (MBP-Htt17$Q_{17}$-ex1) (36). Complementing these in vitro experiments, various computational methods investigated the configurational ensemble of Htt17 and its impact on $Q_N$ at the atomic level. While some observe that Htt17 forms an $\alpha$-helix in aqueous solution by its own (37) and attached to $Q_N$ (38), most observe that Htt17 is, for the most part, unstructured by its own (34,39–41) and attached to $Q_N$ (34,42,43). Htt17 also modulates the structure (34,40) and the aggregation (44) of $Q_N$ oligomers.

In apolar solution, there is a significant increase of the $\alpha$-helix population as shown by CD spectroscopy when adding trifluoroethanol, dodecylphosphocholine (DPC) detergent micelles, or lipid vesicles to aqueous buffers (20,24,35). Early studies postulated that Htt17's ability to form an $\alpha$-helix upon binding to a phospholipid bilayer is encoded in its amphipathic amino acid sequence (20). Indeed, as an $\alpha$-helix, the Htt17 has all its nonpolar amino acids lying on one side separated from the charged amino acids by a well-defined hydrophobic plane. Recent solution NMR experiments by Michalek et al. (35) further unveiled the atomic structure of Htt17 in a DPC micelles solution, showing that it forms a well-structured $\alpha$-helix from residues 6 to 17, while the first five residues are disordered. After these results, the orientation of this model on POPC bilayers has been determined using the $^{15}N$ chemical shifts of $Leu^{7}$, $Phe^{11}$, and $Phe^{17}$ as well as the deuterium quadrupolar splitting of $^{2}H_3$-$Ala^{10}$ obtained by solid-state NMR (45). The Htt17 insertion depth on a phospholipid bilayer has also been recently investigated from the fluorescence intensity quenching of three key residues ($Met^{1}$, $Phe^{11}$, and $Phe^{17}$) mutated to tryptophan (46). Other experiments focused on the membrane interactions of Htt17 when linked to $Q_N$ revealing, for instance, that Htt17 is crucial for $Q_N$ binding and aggregation on membrane bilayers (47), and that it binds more favorably to curved (48) and acidic phospholipid-containing (49) bilayers as the $Q_N$ segment's length increases (49,50).

The structure and dynamics of Htt17 on a phospholipid membrane at the atomic level has also been investigated using atomistic molecular dynamics (MD) simulations. The binding of Htt17, Htt17$Q_{10}$, and Htt17$Q_{20}$ as well as their stability as an $\alpha$-helix on a POPE membrane has been simulated (41). Upon binding to the membrane, the Htt17 segment partitions its nonpolar amino acids inside the hydrophobic core of the membrane, while $Q_N$ remains above the phospholipid headgroups. The role of the $Q_N$ region is to stabilize the Htt17 membrane anchor, easing its insertion as a stable single $\alpha$-helix in agreement with previous experimental observations (35,45). Another group focused on the binding of $KKQ_{35}KK$, $KKQ_{35}P_{11}KK$, Htt17$Q_{35}KK$, and Htt17$Q_{35}P_{11}KK$ from disordered states on a DOPC bilayer (43). They observed that binding of these sequences leads to perturbations of the bilayer physical properties. Htt17 enhances the membrane interactions of huntingtin N-terminal in agreement with previous experiments (47). Both of these computational studies show that Htt17 folding on a bilayer from disordered states occurs beyond the microsecond timescale and involves a slow configurational change (41,43).

With the publication of the NMR model (35,45), we decided to refine the atomistic picture of Htt17 interactions and dynamics on a POPC bilayer using all-atom MD and Hamiltonian replica-exchange (HREX) simulations. We specifically analyze questions of fundamental importance that still need to be addressed.

1. Is the NMR model obtained in the presence of DPC micelles more structured on a POPC bilayer?
2. What are the most significant Htt17-membrane interactions?
3. What is the insertion depth of each residue?
4. What are the bilayer perturbations induced by a structured Htt17 membrane anchor?

Such knowledge is valuable to gain understanding of the atomistic basis of huntingtin interaction with membrane-containing organelles of the cell through its amino-terminus membrane anchor (Htt17). It further provides the necessary information to develop rationales for modulating the localization and aggregation of huntingtin in the cell at the atomic level.

## MATERIALS AND METHODS

In this study, we combine MD and HREX simulations, respectively, of 26 and 20 $\mu$s in total, as summarized in Table 1, to investigate the configurational ensemble of the 17-amino-acid amino-terminus segment (Htt17) of the huntingtin protein on a POPC (1-palmitoyl-2-oleoyl-*sn*-glycero-3-phosphocholine) bilayer. The amino acids sequence of Htt17 is MATLEKLMKAFESLKSF-$NH_2$, where we use an amidated carboxy-terminus as in the NMR experiments to which we compare and then combine our results (35,45).

All simulations are performed using the GROMACS software (ver. 4.6.5) (51–54) combined with the PLUMED plug-in (ver. 2.0.2) for the HREX

**TABLE 1 Summary of the performed simulations**

| Simulations | Phospholipid force field | Type | Initial configuration | Time (ns) |
|---|---|---|---|---|
| Htt17_nmr | Berger | MD | NMR | 1000 × 11 |
| Htt17_$\alpha$ | Berger | MD | $\alpha$ | 1000 × 11 |
| Htt17_nmr_slipids | SLIPIDS | MD | NMR | 1000 × 2 |
| Htt17_$\alpha$_slipids | SLIPIDS | MD | $\alpha$ | 1000 × 2 |
| Htt17_nmr_hrex | Berger | HREX | NMR | 500 × 16 × 1 |
| Htt17_$\alpha$_hrex | Berger | HREX | $\alpha$ | 250 × 16 × 3 |

All simulations are done in the NPT ensemble and are started from the same hexagonal prism periodic cell ($\alpha = 90°$; $\beta = 90°$; $\gamma = 120°$; $a = 7.73$ nm; $b = 7.73$ nm, and $c = 9.24$ nm) containing 8982 water molecules and 167 phospholipids. For the HREX simulation, the number of replicas is 16, as specified in the last column. The AMBER99sb*-ILDN/Berger simulations are presented in the main text, and those using AMBER99sb*-ILDN/SLIPIDS in the Supporting Material. The Htt17_nmr_hrex and two of the Htt17_$\alpha$_hrex simulations are presented in the Supporting Material.

simulations (55,56). The AMBER99sb*-ILDN protein force field (57) is combined with the Berger phospholipid force field (58) as justified in the Supporting Material. The HREX algorithm enhances the sampling by executing simultaneous simulations called replicas with different Hamiltonian (energy) that can exchange, at a given frequency, as specified by the REST2 protocol for which only protein/protein and protein/solvent interactions are scaled (59). In our work, the solvent is the water molecules and phospholipids; therefore, water/water, water/phospholipids, and phospholipids/phospholipids interactions are not scaled. This protocol has been tested on Trp-cage and a $\beta$-hairpin showing a significantly lower computational cost and better sampling than temperature replica exchange (59). Moreover, contrary to temperature replica exchange, this method enhances the sampling of the conformational space at room temperature, which is a necessary condition to conserve the integrity as well as the physical properties of the phospholipid bilayer. For our HREX simulation, we use 16 scales generated by a geometric distribution (and numbered from 1 to 16 in the following order): 1.0, 0.92, 0.85, 0.79, 0.73, 0.67, 0.62, 0.57, 0.53, 0.49, 0.45, 0.41, 0.38, 0.35, 0.33, and 0.3. An exchange between each neighboring scale is attempted every 2 ps, resulting in an exchange rate of 10–30%. More details on this method and on our simulation parameters are provided in the Supporting Material.

The simulations performed in this article are summarized in Table 1. We use two initial states: the NMR model obtained in the presence of DPC micelles (PDB 2LD2) (35), and a single $\alpha$-helix. The NMR model that we use is the third structure in the PDB 2LD2 because it best satisfies the chemical shift constraints obtained by solid-state NMR on a POPC bilayer (45). The other structures are very similar to the third one as STRIDE (60) shows that they all populate disordered configurations from residues 1 to 5 and an $\alpha$-helix from residues 6 to 16 (35). For its part, the single $\alpha$-helix, as its name indicates, has a single $\alpha$-helix running from residues 2 to 16. We use the INFLATEGRO2 procedure with the standard parameters (61) to remove all atomic clashes of the inserted Htt17. Initially, the center-of-mass distance between the backbone atoms of residues 6–17 and the bilayer is 1.8 nm, and the Htt17 lies parallel to the surface of the membrane with its nonpolar residues facing the hydrophobic core of the membrane. We also tested two additional initial positions at 2.0 and 2.5 nm using HREX simulations only. Each MD trajectory and HREX simulation starts from a different velocity distribution after an energy minimization and an NPT equilibration of 10 ns.

## RESULTS

In this section, we analyze more specifically three simulation sets: 11-MD simulations starting from the NMR model (Htt17_nmr), and two separate 11-MD and HREX simulations starting from a single $\alpha$-helix (Htt17_$\alpha$ and Htt17_$\alpha$_hrex, respectively) as summarized in Table 1. We compare, discuss, and combine our results with the experimental measurements obtained by solid-state and two-dimensional solution NMR (35,45) as well as fluorescence (46) spectroscopy. Further comparisons with experimental studies are postponed to the Discussion.

### Htt17 structural stability

We observe that Htt17 remains largely $\alpha$-helical, particularly from residues 7 to 16 in the three simulation sets, with a probability >50% as shown in Fig. 1. The two initial states evolve differently, however. While the NMR model (Htt17_nmr) loses helicity and shows significant fluctuation at residues 6–9, the single $\alpha$-helix (Htt17_$\alpha$ and Htt17_$\alpha$_hrex) is much better preserved overall with a per-residue $\alpha$-helical probability >80% for residues 2–15 with only very small fluctuations. The efficiency of the sampling-enhancing HREX simulation is supported by the fact that the replicas diffuse well (10–30% of exchange acceptance) and that the peptide unfolds at larger scales corresponding to reduced interactions (see Fig. S1 in the Supporting Material). Furthermore, starting from different insertion depths does not change the innate stability of the $\alpha$-helix, which converges to the same equilibrium values for secondary structure, water accessibility, insertion depth, and membrane properties (Fig. S2).

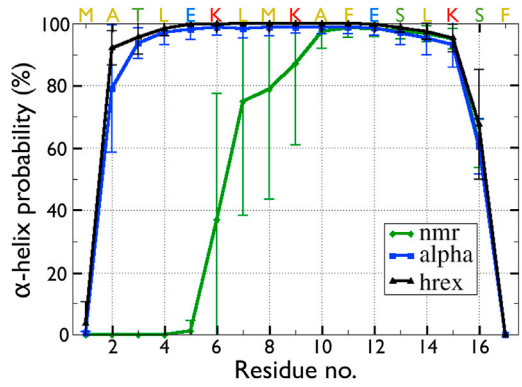


FIGURE 1 Per-residue $\alpha$-helix probability of Htt17. Results for the MD simulations starting from a single $\alpha$-helix and the NMR model determined in the presence of DPC micelles are respectively shown by *blue squares* and *green diamonds*. (*Black triangles*) HREX simulation. Initially, according to STRIDE (60), the NMR model has an $\alpha$-helix from residues 6 to 16 and the $\alpha$-model from residues 2 to 6. The HREX simulation is launched from the $\alpha$-model. The value and the error bar measurements for each residue are, respectively, the average and the standard deviation over all the averages on the 250–1000 ns time interval obtained from 11 independent MD simulations (Table 1). For HREX, the average and standard deviation are computed at the unscaled replica on the 50–250 ns time interval using 20-ns time windows. See Figs. S2 and S3 for the results on the two additional HREX simulations starting from the single $\alpha$-helix at different insertion depths and the one starting from the NMR model, respectively. To see this figure in color, go online.

By comparison with the single $\alpha$-helix, the NMR model is less stable as indicated by the relatively large error bars at residues 6–9. This can be explained by the fact that the helical structure unfolds (turn-and-coil) for these residues in some of the MD trajectories. A HREX simulation starting from the NMR model (Htt17_nmr_hrex) shows even more unfolding of the conformation initially (Fig. S3). Interestingly, however, the Htt17 refolds in this simulation toward a single $\alpha$-helix near the end of the simulation. The sampling enhancing technique HREX seems, in contrast to the MD simulations, to be efficient enough to refold the Htt17 peptide on the bilayer. A longer simulation time, as of this writing beyond our accessible computational resources, will be needed to reach convergence and confirm this observation.

These results suggest that Htt17 could be more structured on a bilayer than the micelle NMR model, which

has rather flexible amino-terminus residues (35). This is supported by tryptophan fluorescence results, indicating a relatively deep penetration of the first residue of Htt17 (46). Moreover, solid-state NMR measurements of Htt17 reconstituted into oriented phospholipid bilayers show a small nonzero $^2$H splitting for Ala$^2$, suggesting structure/interaction with the membrane (E.S.S. and B.B., unpublished observation). This small splitting could either be due a high degree of motion and/or an alignment of the $C_\alpha$-$C_\beta$ vector close to the magic angle. Our simulations also find, in agreement with solid-state NMR (ssNMR), a small quadrupolar splitting for Ala$^2$ (Table 2). This confirms that the magnitude of this value is due in part to a stable $\alpha$-helical conformation around this residue, and in part to a higher degree of motions for Ala$^2$ compared to residues 6–15, as indicated by the fluctuations in the $\alpha$-helical content (Fig. 1).

As expected, the remaining part of the structure, which forms a stable $\alpha$-helix, is very similar to the solution NMR model (35,45) with a backbone root-mean-square deviation on residues 6–16 of 0.11 ± 0.07 nm (Htt17_nmr), 0.07 ± 0.01 nm (Htt17_$\alpha$), and 0.07 ± 0.01 nm (Htt17_$\alpha$_hrex). We also note that residue 17 could be considered part of the helix, because main-chain hydrogen bonds between this residue and residues 13 or 14 are populated 68 ± 5% of the time in Htt17_nmr, 70 ± 4% in Htt17_$\alpha$, and 69 ± 7% in Htt17_$\alpha$_hrex. This is in agreement with the NMR spectra that show nuclear Overhauser effects up to residue 17 and the ssNMR spectra that exhibits an anisotropic $^{15}$N chemical shift at this residue (35,45).

## Htt17 orientation

In terms of orientation, we compare our simulations to ssNMR measurements on the $^{15}$N chemical shifts of Leu$^7$, Phe$^{11}$, Leu$^{14}$, and Phe$^{17}$, and the $^2H_3$ quadrupolar splittings of Ala$^2$ and Ala$^{10}$ of Htt17 on a POPC bilayer (35,45). These values depend, respectively, on the orientation of the C–N and N–H bonds ($^{15}$N), and the $C_\alpha$-$C_\beta$ bond ($^2$H) with respect to the bilayer normal that is aligned in the same direction as the magnetic field (62–64). The computations are described in detail in the Supporting Material.

The averaged chemical shifts and quadrupolar splittings sampled during the Htt17_nmr, Htt17_$\alpha$, and Htt17_$\alpha$_hrex simulations are presented in Table 2. The $^{15}$N-Phe$^{11}$, $^{15}$N-Leu$^{14}$, and $^{15}$N-Phe$^{17}$ chemical shifts and the $^2H_3$-Ala$^2$ quadrupolar splitting for the three simulation sets show good agreement with ssNMR measurements. The signal for $^{15}$N-Leu$^7$ favors instead the $\alpha$-helical configuration over the NMR model that becomes disordered around this residue in our simulations (Htt17_nmr in Fig. 1). Strangely, however, the $^2H_3$-Ala$^{10}$ quadrupolar splitting sampled in the three simulation sets is significantly larger than the experimental measurement. Using a different force field (AMBER99sb*-ILDN/SLIPIDS) yields a value for the $^2H_3$-Ala$^{10}$ quadrupolar splitting that is closer to the experiment, but that is still different (17 ± 1 vs. 11 ± 1 kHz for ssNMR; see Table S1 in the Supporting Material). For the single $\alpha$-helix, this difference could be due to very local structural fluctuations of modest amplitude because the chemical shifts of Ala$^{10}$'s neighboring residues ($^{15}$N-Leu$^7$, $^{15}$N-Phe$^{11}$, and $^{15}$N-Phe$^{17}$) agree with the experimental values. Moreover, this part of the peptide samples similar secondary structure propensity in all simulations, suggesting a very stable global conformation (Fig. 1). These observations are reinforced by two supplementary HREX simulations starting from a less inserted single $\alpha$-helix that yield very similar chemical shifts and quadrupolar splitting (Table S1).

We can further describe the orientation of Htt17 on a bilayer in terms of the tilt and rotational pitch angles as shown in Table 2. These angles are defined as a rotation of Htt17 structure's amphipathic plane, initially in the $x$,$z$ plane, around the negative $z$ axis (rotational pitch) followed by the rotation around the negative $y$ axis (tilt) as shown in Fig. 2 *A*. Using this definition, a rotation of 90° tilt and 90° pitch results in the hydrophobic plane being parallel to the membrane surface ($x$,$y$ plane). These angles can be extracted by the values of $^{15}$N chemical shifts and $^2$H quadrupolar splitting. In particular, the tilt angle depends more strongly on the $^{15}$N shift (62). Here, the good agreement between simulations and ssNMR in the $^{15}$N chemical shifts indicates that the helix axis of Htt17 has an in-plane orientation in the membrane (Table 2).

**TABLE 2 Orientation of Htt17 on the bilayer**

| Simulations | $^2H_3$-Ala$^2$ kHz | $^{15}$N-Leu$^7$ ppm | $^2H_3$-Ala$^{10}$ kHz | $^{15}$N-Phe$^{11}$ ppm | $^{15}$N-Leu$^{14}$ ppm | $^{15}$N-Phe$^{17}$ ppm | Tilt degree | Pitch degree |
|---|---|---|---|---|---|---|---|---|
| Htt17_nmr | 14 ± 20 | 110 ± 28 | 26 ± 12 | 91 ± 3 | 77 ± 6 | 80 ± 15 | 94 ± 5 | 76 ± 5 |
| Htt17_$\alpha$ | −7 ± 10 | 71 ± 2 | 30 ± 6 | 85 ± 1 | 66 ± 1 | 87 ± 4 | 87 ± 5 | 85 ± 5 |
| Htt17_$\alpha$_hrex | −4 ± 7 | 68 ± 3 | 27 ± 8 | 84 ± 1 | 65 ± 2 | 92 ± 5 | 91 ± 5 | 95 ± 5 |
| ssNMR (exp) | 5 ± 2 | 71.2 ± 1.7 | 11 ± 2.5 | 78.9 ± 1.5 | 73.3 ± 1.2 | 88.2 ± 0.9 | 103 ± 5 | 137 ± 5 |

The $^{15}$N chemical shifts of Leu$^7$, Phe$^{11}$, Leu$^{14}$, and Phe$^{17}$ as well as the $^2H_3$ quadrupolar splittings of Ala$^2$ and Ala$^{10}$ are used to extrapolate the orientation of the membrane anchor on the bilayer in terms of tilt and rotational pitch angles (62–64). The ssNMR measurements of Htt17 were done on a POPC bilayer and the tilt and pitch angles were determined for the NMR structure of Htt17 in the presence of DPC micelles (35,45). For the MD simulations, values and their error bar are, respectively, the average and the standard deviation over all the averages on the 250–1000 ns time interval obtained from 11 independent simulations (Table S1). For the HREX simulation, the average and standard deviation are computed at the unscaled replica on the 50–250 ns time interval using 20-ns time windows. See Table S1 for the results on the two additional HREX simulations starting from the single $\alpha$-helix at different insertion depths.

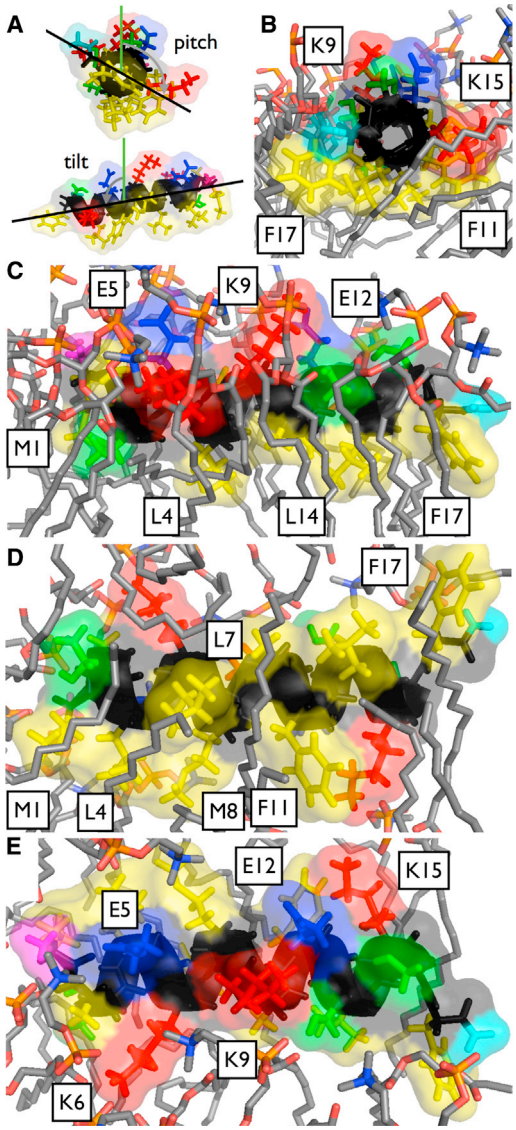


FIGURE 2 Representative structure of the average orientation of Htt17 on a POPC bilayer from the MD trajectory Htt17_$\alpha$. The corresponding $^{15}$N chemical shifts would be 71 (Leu$^{7}$), 85 (Phe$^{11}$), and 87 (Phe$^{17}$) ppm, and the $^{2}H_3$-Ala$^{10}$ quadrupolar splitting is 30 kHz corresponding to a tilt angle of 87 $\pm$ 5° and rotational pitch angle of 85 $\pm$ 5°. (*A*) Graphical definition of the tilt and rotational pitch angles, (*B*) view from the carboxy-terminus, (*C*) view from the side, (*D*) view from the membrane, and (*E*) view from the aqueous solution. The nonpolar (*yellow*), negatively charged (*blue*), positively charged (*red*), and polar (*green*) amino acids of Htt17. (*Black*) Backbone atoms; (*pink*) amino- and (*teal*) carboxy-terminus. To see this figure in color, go online.

The rotational pitch angle, for its part, is a more difficult quantity to extract because it depends on the $^{2}$H quadrupolar splitting, a value that is very sensitive upon local structural changes as observed from experiments and simulations (65,66). In our simulations, the hydrophobic plane of Htt17 is oriented parallel to the membrane surface (pitch ~90°) as expected for an amphipathic monomer such as Htt17 (63). This value differs significantly from the experimentally determined pitch angle (137°), which suggests that the charged residues of Htt17 are preferentially oriented toward the right when looking along the helix axis through the carboxy-terminus (such a point of view is shown in Fig. 2 *B*). This asymmetrical orientation was justified by the possible formation of Htt17 dimers on the bilayer during the ssNMR experiment through electrostatic interactions (35,45). However, introducing small conformational changes to the micellar NMR structure could also result in a more symmetric alignment while at the same time satisfying all solid-state NMR constraints.

Our simulations can be further used to characterize the global motion of the Htt17 helix. We observe that the wagging motion along the helix long axis spreads by a standard deviation of ~8–10°, while the wobbling motion around the helix long axis spreads by a standard deviation of ~14° (data not shown). These angular deviations are quite close to those used for the restriction analysis of the solid-state NMR data where standard deviations of 10° and 18°, respectively, were used for the analysis (35,45). This motional regime used for the analysis of tilt and pitch angles, which is confirmed by the MD results, better represents the situation in a liquid crystalline bilayer than does a completely static peptide, which led to differences of up to ~5°.

## Htt17 interactions with the bilayer

After characterizing Htt17's structural and topological properties, we now examine its interactions with the POPC bilayer. In terms of solvent accessibility, we observe the sequestration of key nonpolar residues such as Leu$^{7}$, Phe$^{11}$, Leu$^{14}$, and Phe$^{17}$ for the three simulation sets (Fig. 3). Moreover, residues involved in frequent hydrogen bonds or salt-bridges with the phosphate group of the phospholipids (Lys$^{6}$, Ser$^{13}$, and Lys$^{15}$, see Table 3) are also more isolated from the solvent. As expected, those that weakly interact with the bilayer (Glu$^{5}$, Lys$^{9}$, and Glu$^{12}$) are highly accessible to the solvent. For the Htt17_$\alpha$ and Htt17_$\alpha$_hrex simulations, residues 1–4 are less accessible to the solvent compared to Htt17_nmr for which these residues are and stay disordered (Fig. 1). Measurements of Htt17 insertion depth in the bilayer support these observations (Fig. 3).

Our simulations can be combined with recent experimental observations (45,46). First, the addition of hydrophilic ($Mn^{2+}$ ions) or hydrophobic (16-doxyl-stearic acid) paramagnetic relaxation reagents in the presence of DPC micelles indicate that residues Leu$^{7}$, Met$^{8}$, Ala$^{10}$, and Phe$^{11}$ of Htt17 are oriented toward the hydrophobic environment of the micelle (45). Our results correlate well with these measurements and confirm that these residues are also strongly involved in the association of Htt17 with a POPC bilayer (Fig. 3). Second, using fluorescence intensity quenching, the insertion depth of residues Met$^{1}$, Phe$^{11}$, and Phe$^{17}$ mutated to tryptophan was measured in the presence of POPC-POPS vesicles containing brominated POPC lipids (46). The relative positions of M1W, F11W, and F17W

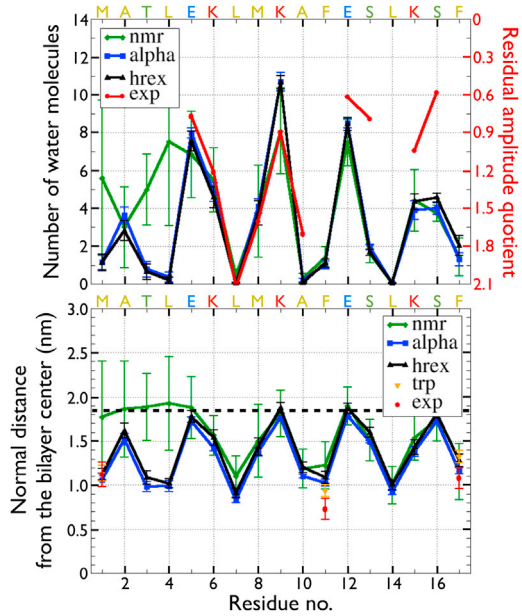


FIGURE 3 Solvent accessibility and insertion depth of each residue of Htt17. (*Top panel*) (*Left-hand side axis*) The solvent accessibility is quantified in terms of the number of water molecules within 0.35 nm from each residue. (*Right-hand side axis*) Residual amplitude quotient due to the addition of hydrophilic ($Mn^{2+}$ ions) and hydrophobic (16-doxyl-stearic acid) paramagnetic relaxation reagents on Htt17 in the presence of DPC detergent micelles (45). A larger residual amplitude quotient indicates a larger solvent accessibility of the side chain. (*Bottom panel*) The insertion depth corresponds to the center-of-mass distance between each side chain and the bilayer along the direction perpendicular to the membrane surface ($z$ axis). (*Dotted line* at 1.8 nm) Average position of the phosphorous atoms of the upper leaflet with respect to the center of the bilayer. The experimental values were measured using fluorescence quenching of Htt17 tryptophan mutants in the presence of POPC/POPS vesicles containing brominated POPC lipids (46). Results for the MD simulations starting from the NMR model (*green diamonds*) and a single $\alpha$-helix (*blue squares*). The HREX simulation (*black triangles*) and the average position (*orange triangles*) of the aromatic rings obtained from direct M1W, F11W, and F17W mutations on the wild-type trajectory. The value and the error bar for each residue, are respectively, the average and the standard deviation over all the averages on the 250–1000 ns time interval obtained from 11 independent MD simulations (Table 1). For HREX, the average and standard deviation are computed at the unscaled replica on the 50–250 ns time interval using 20-ns time windows. See Fig. S2 for the results on the two additional HREX simulations starting from the single $\alpha$-helix at different insertion depths. To see this figure in color, go online.

in Htt17 were measured to 1.12 ± 0.14 nm, 0.73 ± 0.12 nm, and 1.08 ± 0.12 nm, respectively, from the center of the bilayer. Our results from the Htt17_$\alpha$ and Htt17_$\alpha$_hrex simulations agree with the measurement on $Met^{1}$, while $Phe^{17}$ and $Phe^{11}$ are slightly farther from the bilayer center in our simulations (Fig. 3). Because the tryptophan fluorescence transition dipole is probably associated with the aromatic ring only, we now investigate the effect of having tryptophan instead of the wild-type residues on the insertion depth measurements. To do this, we performed the M1W, F11W, and F17W mutations in the Htt17_$\alpha$_hrex wild-type trajectories and optimized the side-chain orientation using SCRWL4 (67). Of course, structural/topological alterations could be introduced by the mutations themselves, but simply taking into account the tryptophan side chain's geometry leads to 1.13 ± 0.09 nm (M1W), 0.93 ± 0.07 nm (F11W), and 1.32 ± 0.07 nm (F17W), which is in better agreement with the experimental measurements. Two supporting HREX simulations starting from a single $\alpha$-helix at different insertion depths (2.0 and 2.5 nm from the bilayer's center, compared to 1.8 nm previously) converge to the same equilibrium values (Fig. S2).

The Htt17 membrane anchor has six residues that can form side-chain hydrogen bonds as donors—$Thr^{3}$, $Lys^{6}$, $Lys^{9}$, $Ser^{13}$, $Lys^{15}$, and $Ser^{16}$—with the oxygens of the phosphate group and the carboxyl groups of POPC. The average number and occurrence probability of H-bonds are shown in Table 3. Ordering these residues in terms of their propensity to form H-bonds yields the following: $Ser^{16} < Thr^{3} < Ser^{13} < Lys^{9} < Lys^{6} \lesssim Lys^{15}$ in Htt17_nmr, $Ser^{16} < Lys^{9} <$ Ser13 $< Thr^{3} < Lys^{15} \lesssim Lys^{6}$ in Htt17_$\alpha$, and $Ser^{16} < Lys^{9} < Thr^{3} < Ser^{13} < Lys^{15} < Lys^{6}$ in Htt17_$\alpha$_hrex. For the two initial states, $Ser^{16}$ shows the lowest H-bond occurrence probability with only 10%, while $Lys^{6}$ and $Lys^{15}$ form H-bonds >85% of the time. Two supporting HREX simulations starting from a single $\alpha$-helix at different insertion depths (2.0 and 2.5 nm from the bilayer's center, compared to 1.8 nm previously) converge to a similar hydrogen-bond interaction pattern (Table S2).

The positively charged lysines of Htt17 also form salt-bridges with the negatively charged phosphate group of the phospholipids. With occurrence probabilities ranging from 28 to 60%, we see that such salt-bridges are a key component of the interactions between Htt17 and the bilayer (Table 3). Moreover, these residues can participate in up to three salt-bridges with different phospholipids. In order of occurrence probability, we find $Lys^{9} < Lys^{6} \lesssim Lys^{15}$ in Htt17_nmr, and $Lys^{9} < Lys^{15} < Lys^{6}$ for the single $\alpha$-helix in both Htt17_$\alpha$ and Htt17_$\alpha$_hrex. While $Lys^{9}$ has a lower probability to form salt-bridges with the phospholipids, contrary to the other lysines it often forms intramolecular salt-bridges with either $Glu^{5}$ or $Glu^{12}$ (Table S4). In principle, the negatively charged glutamic acids of Htt17 could form salt-bridges with the positively charged nitrogen of the choline group. However, the occurrence probability for such salt-bridges is very low (1–2%) because the three methyl groups surrounding the nitrogen cause steric hindrance to the salt-bridge formation (Table 3). Two supporting HREX simulations starting from a single $\alpha$-helix at different insertion depths (2.0 and 2.5 nm from the bilayer's center, compared to 1.8 nm previously) converge to a similar salt-bridge interaction pattern (Table S3).

## DISCUSSION

The first 17 amino acids at the amino-terminus (Htt17) of huntingtin, a large protein related to Huntington's disease

**TABLE 3 Average number of hydrogen bonds and salt-bridges between Htt17 and the phospholipids of the membrane**

| Interaction type | Residue | Htt17_nmr number (%) | Htt17_$\alpha$ number (%) | Htt17_hrex number (%) |
|---|---|---|---|---|
| Hydrogen bonds | $Thr^{3}$ | 0.9 ± 0.3 (14 ± 19) | 1.0 ± 0.0 (61 ± 30) | 1.0 ± 0.0 (51 ± 30) |
| | $Lys^{6}$ | 1.8 ± 0.3 (85 ± 17) | 1.9 ± 0.2 (92 ± 4) | 2.2 ± 0.2 (95 ± 5) |
| | $Lys^{9}$ | 1.4 ± 0.2 (56 ± 19) | 1.4 ± 0.2 (38 ± 11) | 1.1 ± 0.1 (32 ± 9) |
| | $Ser^{13}$ | 1.0 ± 0.0 (45 ± 22) | 1.0 ± 0.0 (54 ± 8) | 1.0 ± 0.1 (54 ± 19) |
| | $Lys^{15}$ | 1.8 ± 0.3 (86 ± 8) | 1.7 ± 0.1 (90 ± 4) | 1.7 ± 0.2 (90 ± 3) |
| | $Ser^{16}$ | 1.0 ± 0.0 (9 ± 5) | 1.0 ± 0.0 (6 ± 2) | 1.0 ± 0.1 (5 ± 4) |
| Salt-bridges | $Glu^{5}$ | 0.9 ± 0.3 (1 ± 2) | 1.0 ± 0.0 (1 ± 1) | 1.0 ± 0.1 (1 ± 1) |
| | $Glu^{12}$ | 0.9 ± 0.3 (1 ± 1) | 1.0 ± 0.0 (1 ± 0) | 1.0 ± 0.0 (1 ± 1) |
| | $Lys^{6}$ | 1.1 ± 0.1 (49 ± 11) | 1.2 ± 0.1 (60 ± 8) | 1.3 ± 0.2 (65 ± 20) |
| | $Lys^{9}$ | 1.2 ± 0.1 (40 ± 13) | 1.1 ± 0.0 (28 ± 5) | 1.1 ± 0.1 (28 ± 7) |
| | $Lys^{15}$ | 1.1 ± 0.1 (51 ± 8) | 1.1 ± 0.1 (48 ± 9) | 1.0 ± 0.1 (38 ± 10) |

For a given residue, statistics are performed only over the frames in which the residue forms at least one H-bond or salt-bridge. The numbers in parentheses represent the probability of occurrence in percentage. The value and the error bar for each residue are, respectively, the average and the standard deviation over all the averages on the 250–1000 ns time interval obtained from 11 independent MD simulations (Tables S2 and S3). For the HREX simulation, the average and standard deviation are computed at the unscaled replica on the 50–250 ns time interval using 20-ns time windows. See Tables S2 and S3 for the results on the two additional HREX simulations starting from the single $\alpha$-helix at different insertion depths.

and with multiple biological functions (5–9), modulate its localization, function, aggregation, and degradation in the cell (20–29). For instance, the amphipathic character of the Htt17 segment is responsible for huntingtin's membrane anchoring properties and regulates its interaction with specific membrane-containing organelles of the cell (20). Recently, solution NMR has been used to resolve the structure of Htt17 in the presence of DPC detergent micelles (35). Solid-state NMR further unveiled its orientation on a POPC bilayer using $^{15}N$ chemical shift and $^{2}H$ quadrupolar splitting measurements (45).

The MD and HREX simulations described in this article are combined with these NMR measurements to yield the first high-resolution model for the membrane-anchoring properties of the Htt17 segment of huntingtin. Our results refine the atomistic picture of Htt17 on a phospholipid bilayer in terms of its structure, orientation, key membrane interactions (hydrogen bonds, salt-bridges, insertion depth, and solvent accessibility), and membrane perturbations (order parameter, area per lipid, and thickness), as well as the influence of the phospholipid type on those observations. We now discuss each finding and their implications in detail.

## The Htt17 monomer forms a stable $\alpha$-helix on a POPC bilayer

In aqueous solution, the Htt17 monomer is mostly disordered as shown by solution NMR (24), while CD spectroscopy suggests that it can form transient helical structures (20,24,34,35). Transition to a stable $\alpha$-helix occurs upon self-association (31) as well as upon addition of phospholipid vesicles, detergent micelles, or apolar compounds to an aqueous buffer (20,24,35). Recently, the structure of Htt17 in the presence of DPC micelles has been resolved using solution NMR spectroscopy: it is disordered from residues 1 to 5 and it is an $\alpha$-helix for the rest of the sequence (35). Despite indirect indications from ssNMR (45), it had not yet been verified whether Htt17 adopts exactly the same structure on a phospholipid bilayer.

Our simulations extend previous observations by showing, with many independent MD and HREX simulations, that the first residues of Htt17 also form a stable $\alpha$-helix on a POPC bilayer (Fig. 1). Moreover, the $^{15}N$ chemical shifts of $Leu^{7}$, $Phe^{11}$, and $Phe^{17}$ sampled during those simulations agree with solid-state NMR measurements of Htt17 on a POPC bilayer (45) (Table 2). These values are consistent with an in-plane orientation of the amphipathic Htt17 with respect to the membrane surface, as depicted in Fig. 2. Our observations are further supported by very similar results obtained in terms of structure (Fig. S4) and chemical shifts (Table S1) using a different force field (AMBER99sb*-ILDN/SLIPIDS, Table 1).

The increased stability of the Htt17 monomer as an $\alpha$-helix due to the presence of a phospholipid bilayer could have a strong impact on its oligomerization. In aqueous solution, Htt17 is mostly disordered at the monomeric level as shown by solution NMR experiment (24), but it forms a stable tetrameric bundle of four $\alpha$-helical Htt17 (31). When linked to the polyglutamine segment ($Q_N$) that follows Htt17 in huntingtin's sequence, the aggregation pathway of $Q_N$ is significantly modified (31,32). More precisely, Htt17$Q_N$ has two main aggregation pathways in direct kinetic competition: 1) one is initiated by the formation of $\alpha$-helical tetrameric bundles of Htt17 that combine to form larger oligomeric assemblies favoring $Q_N$ fibrillation due to an increase in its local concentration, and 2) the other is independent of structure formation in Htt17 resulting in an aggregation pathway that is very similar to $Q_N$ alone (32). The first pathway yields faster fibrillation kinetics (24,30).

Here, we observe that the Htt17 monomer forms a stable $\alpha$-helix on the bilayer (Fig. 1) that is significantly different from its mostly disordered structure in aqueous solution as observed from other simulations using the same force field

(41). The presence of the membrane favors the formation of $\alpha$-helical structures in Htt17 that could then ease the nucleation of the $\alpha$-helical tetrameric bundle of Htt17. Consequently, the oligomerization and fibrillation kinetics of Htt17$Q_N$ could be enhanced by the presence of a phospholipid bilayer (35) as for other amyloidogenic proteins (68). On the membrane, as observed from MD simulations, the $Q_N$ region of Htt17$Q_N$ and Htt17$Q_NP_{11}$ is indeed easily available for aggregation, because it lies on the surface of the phospholipid heads (41,43) and weakly interacts with Htt17 (41). The converse argument is also possible: the formation of oligomeric structures containing an $\alpha$-helical Htt17 before its binding on the phospholipid bilayer could favor its insertion. Indeed, previous simulations suggest that the complete partitioning of Htt17 nonpolar residues is eased by the presence of $\alpha$-helical structures before binding, while the reordering of disordered structures on the bilayer are impeded by strong electrostatic interactions between Htt17 and the phospholipids (41).

## The key residues for Htt17-membrane interaction are crucial to huntingtin's function

The Htt17 segment of huntingtin is involved in several posttranslational modifications such as SUMOylation (25) and phosphorylation (26–29) that are crucial to its physiological and pathological functions. More precisely, SUMOylation implicating $Lys^6$ and $Lys^9$ correlates with increased neurodegeneration in *Drosophila*, possibly through the modulation of huntingtin localization and aggregation (25). Phosphorylation of $Ser^{13}$ and $Ser^{16}$ increases huntingtin clearance, reduces the toxicity in a mouse model, regulates other posttranslational modifications of Htt17, and increases nuclear localization of huntingtin (26,28,29). Phosphorylation of $Thr^3$ increases the formation of insoluble aggregates and a phosphomimetic mutation of the threonine to an aspartic acid reduces the neurodegeneration in *Drosophila* (27). Mutations or truncations of the nonpolar residues implicated in the nuclear export signal of Htt17—L4, L7, F11, and L14—lead to a significant increase of huntingtin accumulation in the nucleus (20,22,69). Neutralization of the lysines and glutamic acids by substitution to alanines modulates the membrane composition targeted by Htt17 (20).

In our simulations, we observe that many of these crucial residues are involved in specific interactions with the phospholipids. For instance, salt-bridges between $Lys^6$ and $Lys^{15}$ and the phospholipids occur often, while $Lys^9$ is mainly involved in intramolecular salt-bridges with either of the two glutamic acids in Htt17 (Tables 3 and S4). These charged residues as well as $Ser^{13}$ also regularly form hydrogen bonds with the phospholipids (Table 3). Moreover, nonpolar sequestration of L7, F11, and L14 inside the hydrophobic core of the membrane is crucial to the anchoring of Htt17 (Fig. 3). Our observations are reinforced by similar results in terms of solvent accessibility (Fig. S5), insertion depth (Fig. S6), hydrogen bonds (Table S2), and salt-bridges (Table S3) using a different force field (AMBER99sb*-ILDN/SLIPIDS, Table 1). Our simulations therefore suggest that perturbation of these key membrane interactions (Table 3 and Fig. 3) will likely impact Htt17's ability for membrane binding in various ways, consequently affecting huntingtin localization in the cell and potentially its function.

## The network of electrostatic interactions depends on the phospholipid type, but not the configuration of Htt17

The structure and orientation of Htt17 remain almost unchanged when inserted in membranes of different composition as shown from solution NMR, solid-state NMR, and CD spectroscopy (35). In contrast, the ability of this membrane anchor to target phospholipid vesicles highly depends in the membrane composition as shown from the binding affinity extrapolated from CD measurements and tryptophan-emission fluorescence (35,46). More precisely, Htt17 binds more favorably to membranes containing anionic phospholipids such as PS and PG than to the zwitterionic PC, while the presence of cholesterol has the opposite effect. A similar behavior has also been observed for the exon 1 of huntingtin (49).

We can compare our results on a POPC bilayer to a previous study in which we investigated Htt17 on a POPE bilayer using MD simulations (41). Because these simulations were done using the AMBER99sb*-ILDN/SLIPIDS force field, we compare them to the results on the POPC bilayer obtained using the same force field (Table 1). In each case, we have two simulations of 500 ns each for POPE and of 1000 ns each for POPC starting from different velocity distributions. Htt17 is initially a single $\alpha$-helix inserted in the bilayer below the phosphate group of the phospholipids.

We observe that Htt17's structure (Fig. S7) and orientation (Table S5) are quantitatively similar in the zwitterionic POPC and POPE bilayers. In contrast, the insertion depth of Htt17 (Fig. S8) and its network of salt-bridges and hydrogen bonds with the phospholipids (Table S6) are different. More precisely, the main difference is that the glutamic acids ($Glu^5$ and $Glu^{12}$) form salt-bridges and hydrogen bonds with the amine group of PE, while such interactions are not present for the choline group of PC. This shifts Htt17 nearer from the phospholipid heads without changing significantly its solvent accessibility. In the previous simulations on POPE, we also observed that electrostatic interactions initialize the binding of Htt17 on the phospholipid bilayer (41).

Taken together, experiments and simulations suggest that the main interaction responsible for the structure and orientation of Htt17 is the sequestration of its nonpolar residues in the hydrophobic core of the membrane, as

this is independent of the phospholipid species. In contrast, the binding affinity of Htt17 on phospholipid bilayers appears to depend on specific electrostatic interactions that are modulated by the membrane composition. The main role of the charged residues could be to target selectively membrane with specific phospholipid compositions. Indeed, experiment shows that mutating the charged residues to alanines can change the localization of huntingtin in the cell (20).

Besides the phospholipid type, the presence of cholesterol also has an impact: increasing its concentration significantly impedes Htt17's ability to bind and permeabilize phospholipid membranes (35,46). As discussed in the next section, our simulations show that Htt17 induces local perturbations in the physical properties of the bilayer such as membrane thinning, reduced phospholipid area, and decreased phospholipid order parameters (Fig. 4). These perturbations are due to the neighboring phospholipids of Htt17 extending their acyl chains to cover its nonpolar surface (Fig. 4). Experiment show that the effect of cholesterol is the opposite: it increases the order of the phospholipid acyl chains and the membrane thickness. And by doing so, the cholesterol might protect the membrane from accommodating the binding state of the Htt17 monomer, thereby reducing its binding affinity and further oligomerization in the membrane.

## The Htt17 monomer locally perturbs the physical properties of the bilayer

Experiments show that the presence of 2.5 mol % of Htt17 on POPC, POPE/POPG, and POPC/POPS bilayers significantly reduces the order parameters of the phospholipid palmitic chain (35). A few micromoles of Htt17 are sufficient to induce leakage of large POPC and POPC/POPS unilamellar vesicles (35). Globular aggregates of the exon 1 of huntingtin increase the roughness, similarly to other amyloid protein (72), and change the mechanical properties of total brain lipid extract bilayers, as shown by atomic force microscopy (50).

At the monomer level, we observe that the presence of Htt17 on a POPC membrane already leads to local perturbations of the bilayer physical properties as summarized in Fig. 4. For instance, the area per lipid and membrane thickness are decreased within a distance of ~1 nm from Htt17 with respect to the bulk phospholipids. This reordering of the bilayer accommodates Htt17 by allowing its neighboring phospholipids to extend their acyl chain to cover its nonpolar surface as depicted by Fig. 2. The resulting order parameters of these acyl chains is decreased with respect to the membrane bulk (Fig. 4) in agreement with other MD simulation of a disordered KKHtt17$Q_{35}$KK on a DPPC bilayer (43) and with experimental measurements on a POPC bilayer with 2.5 mol % of Htt17 (35).

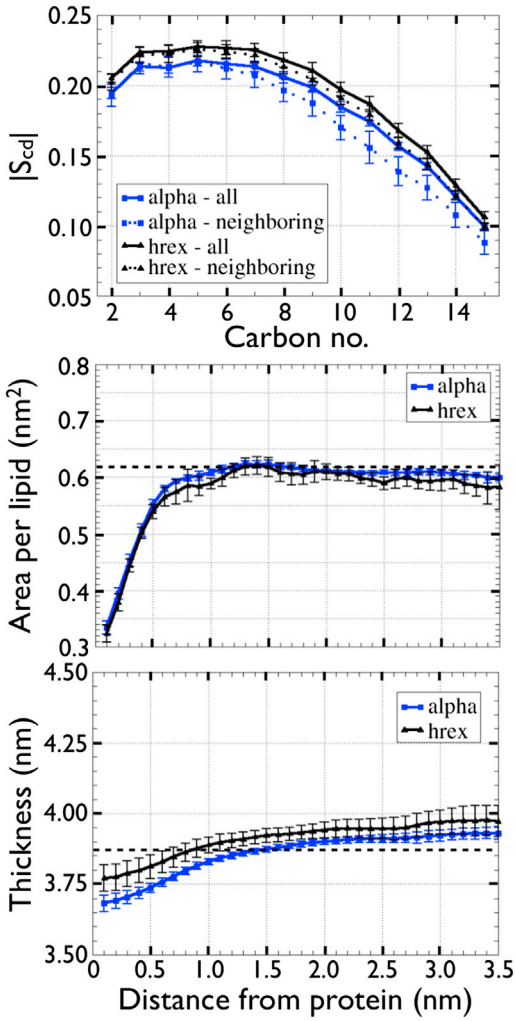


FIGURE 4 Perturbations of the bilayer properties by Htt17. Results for Htt17_$\alpha$ (*blue squares*) and Htt17_$\alpha$_hrex (*black triangles*). (*A*) Average order parameters of the palmitic chain carbons of the neighboring (*dotted*) and then total (*line*) phospholipids. The neighboring phospholipids are defined as those within 1.0 nm of Htt17 in the upper leaflet. (*B*) Average membrane thickness computed using GRIDMAT (70) and (*C*) average area per phospholipid computed using VTMC (71) as a function of their distance from Htt17. (For panels *B* and *C*, the *black dotted line* represents the averaged value for a simulated POPC bilayer without Htt17.) The value and the error bar for each residue are, respectively, the average and the standard deviation over all the averages on the 250–1000 ns time interval obtained from 11 independent MD simulations (Table 1). For the HREX simulation, the average and standard deviation are computed at the unscaled replica on the 50–250 ns time interval using 20-ns time windows. See Fig. S2 for the results on the two additional HREX simulations starting from the single $\alpha$-helix at different insertion depths. To see this figure in color, go online.

Theoretical studies show that such local membrane deformations around a peptide promote dimerization of inserted amphipathic peptides on phospholipid membranes (73–75). This could favor the dimerization and further oligomerization of Htt17. Dimerization could be initiated and stabilized by the formation of electrostatic interactions as

proposed from ssNMR orientation measurements on Htt17 (35). Our simulations indeed show that most of the charged residues stay accessible to the solvent (Fig. 3). We expect the rate-limiting step of such a process to be the need to break the strong peptide-phospholipids interactions (Table 3), as some of the neighboring phospholipids of Htt17 exchange very slowly with the membrane bulk: ~10 phospholipids stay in contact with the peptide for >400 ns and 20 for >150 ns (Fig. S9).

After dimerization, Htt17 could then form (as observed experimentally) larger globular aggregates that significantly change the membrane properties (50) and cause vesicle permeabilization (35,45). However, the preferred mechanism of permeabilization by Htt17—pore formation, carpet model, or detergent model (76)—remains unknown. While pore formation of Htt17 alone is probably not relevant for the biological activities because it is weak in membranes with cholesterol or absent in POPE/POPG membrane (35), it could be different in the presence of the amyloidogenic $Q_N$ region (Htt17$Q_N$). Further integrated experimental and computational studies on this front will be essential to compare huntingtin with the other amyloid proteins that are known to perturb phospholipid membranes (77,78). While the $Q_N$ region can perturb on its own the membrane integrity (79–81), from our results on the Htt17 and Htt17$Q_N$ monomers (41) and previous experimental observations, we suggest a new paradigm: the role of the amyloidogenic $Q_N$ region could be to stabilize, in a length-dependent manner, the oligomeric assemblies of huntingtin exon 1 because it stays on the surface and is easily accessible for oligomerization. The amphipathic Htt17, for its part, could play a fundamental role by initiating the binding and insertion of the monomer in the membrane as well as by perturbing the physical properties of the bilayer in a manner to favor its oligomerization, similarly to other $\alpha$-helical amphipathic peptides (76,82,83).

## CONCLUSIONS

The function and localization of huntingtin are intrinsically dependent on the first 17 amino acids at its amino-terminus (Htt17). This amphipathic segment serves as a membrane anchor and is situated just before the amyloidogenic polyglutamine segment of huntingtin. In this study, we present a high-resolution atomistic model of the Htt17 monomer on a phospholipid bilayer by combining atomistic MD and HREX simulations together with experimental results from solution and solid-state nuclear magnetic resonance, as well as fluorescence spectroscopy. Our model quantifies the key interactions between Htt17 and the phospholipids of the bilayer responsible for its structure, orientation, and insertion depth, as well as the resulting physical perturbation of the bilayer structure. It rationalizes, at the atomic level, the potential effect of different membrane compositions and posttranslational modifications of Htt17 on its ability to target phospholipid bilayers. It also describes the impact of the monomer configuration and membrane perturbations on Htt17 and Htt17$Q_N$ self-association into oligomeric complexes of potential relation to the pathogenesis of huntingtin.

Finally, we observe that the sampling enhancing method HREX, which enables the system to easily move out of local minima that could bias the sampling, is ideal for the peptide-membrane system because it is performed at room temperature, it does not perturb the membrane physical properties, and it speeds up the convergence of the observables. This computational method could be readily applicable to investigate a wider variety of membrane compositions to precisely unveil, at the atomic level, the concentration dependence of cholesterol and charged phospholipids on Htt17, Htt17$Q_N$, and Htt17$Q_N P_{11}$ structure, orientation, key interactions, binding affinity, and oligomerization on the surface of phospholipid membranes.

## SUPPORTING MATERIAL

Supporting Materials and Methods, nine figures, and six tables are available at http://www.biophysj.org/biophysj/supplemental/S0006-3495(15)00127-7.

## AUTHOR CONTRIBUTIONS

S.C., B.B., and N.M. designed the research; S.C. and V.B. performed the research; S.C., V.B., and E.S.S. contributed analytic tools; S.C., V.B., E.S.S., B.B., and N.M. analyzed the data; and S.C., B.B., and N.M. wrote the manuscript.

## ACKNOWLEDGMENTS

The authors thank Giovanni Bussi for his help in setting up the Hamiltonian replica exchange (HREX) simulation.

Computations were made on the computing facilities of Calcul Québec/Compute Canada. The operation of these supercomputers is funded by the Canada Foundation for Innovation, Nano Québec, RMGA, and the Fonds de Recherche Québécois sur la Nature et les Technologies.

This work was funded in part by the Canada Research Chairs program, the Fonds de Recherche Québécois sur la Nature et les Technologies, the Natural Sciences and Engineering Research Council of Canada, and the Fonds de Recherche en Santé du Québec, the Agence Nationale de la Recherche (projects TRANSPEP, ProLinIn, membraneDNP, and the LabEx Chemistry of Complex System), the University of Strasbourg, the Centre National de la Recherche Scientifique, the American Foundation for Research on Huntington's Disease (Cure Huntington's Disease Initiative), and Les Réseaux Thématique de Recherche Avancée International Center of Frontier Research in Chemistry.

## REFERENCES

1. Duyao, M. P., A. B. Auerbach, …, M. E. MacDonald. 1995. Inactivation of the mouse Huntington's disease gene homolog Hdh. *Science.* 269:407–410.

2. Caviston, J. P., and E. L. F. Holzbaur. 2009. Huntingtin as an essential integrator of intracellular vesicular trafficking. *Trends Cell Biol.* 19:147–155.
3. Atwal, R. S., and R. Truant. 2008. A stress sensitive ER membrane-association domain in Huntingtin protein defines a potential role for Huntingtin in the regulation of autophagy. *Autophagy.* 4:91–93.
4. Kegel, K. B., E. Sapp, …, M. DiFiglia. 2005. Huntingtin associates with acidic phospholipids at the plasma membrane. *J. Biol. Chem.* 280:36464–36473.
5. Zheng, Z., and M. I. Diamond. 2012. Huntington disease and the huntingtin protein. *Prog. Mol. Biol. Transl. Sci.* 107:189–214.
6. Zoghbi, H. Y., and H. T. Orr. 2000. Glutamine repeats and neurodegeneration. *Annu. Rev. Neurosci.* 23:217–247.
7. Bates, G. P. 2005. History of genetic disease: the molecular genetics of Huntington disease—a history. *Nat. Rev. Genet.* 6:766–773.
8. Gatchel, J. R., and H. Y. Zoghbi. 2005. Diseases of unstable repeat expansion: mechanisms and common principles. *Nat. Rev. Genet.* 6: 743–755.
9. Orr, H. T., and H. Y. Zoghbi. 2007. Trinucleotide repeat disorders. *Annu. Rev. Neurosci.* 30:575–621.
10. Benn, C. L., C. Landles, …, G. P. Bates. 2005. Contribution of nuclear and extranuclear polyQ to neurological phenotypes in mouse models of Huntington's disease. *Hum. Mol. Genet.* 14:3065–3078.
11. Ritch, J. J., A. Valencia, …, K. B. Kegel. 2012. Multiple phenotypes in Huntington disease mouse neural stem cells. *Mol. Cell. Neurosci.* 50:70–81.
12. DiFiglia, M., E. Sapp, …, N. Aronin. 1997. Aggregation of huntingtin in neuronal intranuclear inclusions and dystrophic neurites in brain. *Science.* 277:1990–1993.
13. Kim, Y. J., Y. Yi, …, M. DiFiglia. 2001. Caspase 3-cleaved N-terminal fragments of wild-type and mutant huntingtin are present in normal and Huntington's disease brains, associate with membranes, and undergo calpain-dependent proteolysis. *Proc. Natl. Acad. Sci. USA.* 98: 12784–12789.
14. Ratovitski, T., M. Nakamura, …, C. A. Ross. 2007. N-terminal proteolysis of full-length mutant huntingtin in an inducible PC12 cell model of Huntington's disease. *Cell Cycle.* 6:2970–2981.
15. Mangiarini, L., K. Sathasivam, …, G. P. Bates. 1996. Exon 1 of the HD gene with an expanded CAG repeat is sufficient to cause a progressive neurological phenotype in transgenic mice. *Cell.* 87:493–506.
16. Davies, S. W., M. Turmaine, …, G. P. Bates. 1997. Formation of neuronal intranuclear inclusions underlies the neurological dysfunction in mice transgenic for the HD mutation. *Cell.* 90:537–548.
17. Cisbani, G., and F. Cicchetti. 2012. An in vitro perspective on the molecular mechanisms underlying mutant huntingtin protein toxicity. *Cell Death Dis.* 3:e382.
18. Zhang, Q. C., T.-L. Yeh, …, M. A. Poirier. 2011. A compact $\beta$ model of huntingtin toxicity. *J. Biol. Chem.* 286:8188–8196.
19. Nucifora, L. G., K. A. Burke, …, M. A. Poirier. 2012. Identification of novel potentially toxic oligomers formed in vitro from mammalian-derived expanded huntingtin exon-1 protein. *J. Biol. Chem.* 287: 16017–16028.
20. Atwal, R. S., J. Xia, …, R. Truant. 2007. Huntingtin has a membrane association signal that can modulate huntingtin aggregation, nuclear entry and toxicity. *Hum. Mol. Genet.* 16:2600–2615.
21. Rockabrand, E., N. Slepko, …, L. M. Thompson. 2007. The first 17 amino acids of Huntingtin modulate its sub-cellular localization, aggregation and effects on calcium homeostasis. *Hum. Mol. Genet.* 16:61–77.
22. Zheng, Z., A. Li, …, M. I. Diamond. 2013. An N-terminal nuclear export signal regulates trafficking and aggregation of Huntingtin (Htt) protein exon 1. *J. Biol. Chem.* 288:6063–6071.
23. Maiuri, T., T. Woloshansky, …, R. Truant. 2013. The huntingtin N17 domain is a multifunctional CRM1 and Ran-dependent nuclear and ciliial export signal. *Hum. Mol. Genet.* 22:1383–1394.
24. Thakur, A. K., M. Jayaraman, …, R. Wetzel. 2009. Polyglutamine disruption of the huntingtin exon 1 N terminus triggers a complex aggregation mechanism. *Nat. Struct. Mol. Biol.* 16:380–389.
25. Steffan, J. S., N. Agrawal, …, J. L. Marsh. 2004. SUMO modification of Huntingtin and Huntington's disease pathology. *Science.* 304: 100–104.
26. Gu, X., E. R. Greiner, …, X. W. Yang. 2009. Serines 13 and 16 are critical determinants of full-length human mutant huntingtin induced disease pathogenesis in HD mice. *Neuron.* 64:828–840.
27. Aiken, C. T., J. S. Steffan, …, J. L. Marsh. 2009. Phosphorylation of threonine 3: implications for Huntingtin aggregation and neurotoxicity. *J. Biol. Chem.* 284:29427–29436.
28. Thompson, L. M., C. T. Aiken, …, J. S. Steffan. 2009. IKK phosphorylates Huntingtin and targets it for degradation by the proteasome and lysosome. *J. Cell Biol.* 187:1083–1099.
29. Atwal, R. S., C. R. Desmond, …, R. Truant. 2011. Kinase inhibitors modulate huntingtin cell localization and toxicity. *Nat. Chem. Biol.* 7:453–460.
30. Liebman, S. W., and S. C. Meredith. 2010. Protein folding: sticky N17 speeds huntingtin pile-up. *Nat. Chem. Biol.* 6:7–8.
31. Jayaraman, M., R. Kodali, …, R. Wetzel. 2012. Slow amyloid nucleation via $\alpha$-helix-rich oligomeric intermediates in short polyglutamine-containing huntingtin fragments. *J. Mol. Biol.* 415:881–899.
32. Jayaraman, M., R. Mishra, …, R. Wetzel. 2012. Kinetically competing huntingtin aggregation pathways control amyloid polymorphism and properties. *Biochemistry.* 51:2706–2716.
33. Wetzel, R. 2012. Physical chemistry of polyglutamine: intriguing tales of a monotonous sequence. *J. Mol. Biol.* 421:466–490.
34. Williamson, T. E., A. Vitalis, …, R. V. Pappu. 2010. Modulation of polyglutamine conformations and dimer formation by the N-terminus of huntingtin. *J. Mol. Biol.* 396:1295–1309.
35. Michalek, M., E. S. Salnikov, …, B. Bechinger. 2013. Membrane interactions of the amphipathic amino terminus of huntingtin. *Biochemistry.* 52:847–858.
36. Kim, M. W., Y. Chelliah, …, I. Bezprozvanny. 2009. Secondary structure of Huntingtin amino-terminal region. *Structure.* 17:1205–1212.
37. Kelley, N. W., X. Huang, …, V. S. Pande. 2009. The predicted structure of the headpiece of the Huntingtin protein and its implications on Huntingtin aggregation. *J. Mol. Biol.* 388:919–927.
38. Długosz, M., and J. Trylska. 2011. Secondary structures of native and pathogenic huntingtin N-terminal fragments. *J. Phys. Chem. B.* 115:11597–11608.
39. Rossetti, G., P. Cossio, …, P. Carloni. 2011. Conformations of the Huntingtin N-term in aqueous solution from atomistic simulations. *FEBS Lett.* 585:3086–3089.
40. Côté, S., G. Wei, and N. Mousseau. 2012. All-atom stability and oligomerization simulations of polyglutamine nanotubes with and without the 17-amino-acid N-terminal fragment of the Huntingtin protein. *J. Phys. Chem. B.* 116:12168–12179.
41. Côté, S., G. Wei, and N. Mousseau. 2014. Atomistic mechanisms of huntingtin N-terminal fragment insertion on a phospholipid bilayer revealed by molecular dynamics simulations. *Proteins.* 82:1409–1427.
42. Lakhani, V. V., F. Ding, and N. V. Dokholyan. 2010. Polyglutamine induced misfolding of huntingtin exon1 is modulated by the flanking sequences. *PLOS Comput. Biol.* 6:e1000772.
43. Nagarajan, A., S. Jawahery, and S. Matysiak. 2014. The effects of flanking sequences in the interaction of polyglutamine peptides with a membrane bilayer. *J. Phys. Chem. B.* 118:6368–6379.
44. Ruff, K. M., S. J. Khan, and R. V. Pappu. 2014. A coarse-grained model for polyglutamine aggregation modulated by amphipathic flanking sequences. *Biophys. J.* 107:1226–1235.
45. Michalek, M., E. S. Salnikov, and B. Bechinger. 2013. Structure and topology of the huntingtin 1-17 membrane anchor by a combined solution and solid-state NMR approach. *Biophys. J.* 105:699–710.

46. Michalek, M., C. Aisenbrey, and B. Bechinger. 2014. Investigation of membrane penetration depth and interactions of the amino-terminal domain of huntingtin: refined analysis by tryptophan fluorescence measurement. *Eur. Biophys. J.* 43:347–360.

47. Burke, K. A., K. J. Kauffman, …, J. Legleiter. 2013. The interaction of polyglutamine peptides with lipid membranes is regulated by flanking sequences associated with huntingtin. *J. Biol. Chem.* 288:14993–15005.

48. Chaibva, M., K. A. Burke, and J. Legleiter. 2014. Curvature enhances binding and aggregation of huntingtin at lipid membranes. *Biochemistry.* 53:2355–2365.

49. Kegel, K. B., E. Sapp, …, M. DiFiglia. 2009. Polyglutamine expansion in huntingtin alters its interaction with phospholipids. *J. Neurochem.* 110:1585–1597.

50. Burke, K. A., K. M. Hensal, …, J. Legleiter. 2013. Huntingtin disrupts lipid bilayers in a polyQ-length dependent manner. *Biochim. Biophys. Acta.* 1828:1953–1961.

51. Pronk, S., S. Páll, …, E. Lindahl. 2013. GROMACS 4.5: a high-throughput and highly parallel open source molecular simulation toolkit. *Bioinformatics.* 29:845–854.

52. Hess, B., C. Kutzner, …, E. Lindahl. 2008. GROMACS 4: algorithms for highly efficient, load-balanced, and scalable molecular simulation. *J. Chem. Theory Comput.* 4:435–447.

53. van der Spoel, D., E. Lindahl, …, H. J. C. Berendsen. 2005. GROMACS: fast, flexible, and free. *J. Comput. Chem.* 26:1701–1718.

54. Berendsen, H. J. C., D. van der Spoel, and R. van Drunen. 1995. GROMACS: a message-passing parallel molecular dynamics implementation. *Comput. Phys. Commun.* 91:43–56.

55. Tribello, G. A., M. Bonomi, …, G. Bussi. 2014. PLUMED 2: new feathers for an old bird. *Comput. Phys. Commun.* 185:604–613.

56. Bussi, G. 2014. Hamiltonian replica exchange in GROMACS: a flexible implementation. *Mol. Phys.* 112:379–384.

57. Piana, S., K. Lindorff-Larsen, and D. E. Shaw. 2011. How robust are protein folding simulations with respect to force field parameterization? *Biophys. J.* 100:L47–L49.

58. Cordomí, A., G. Caltabiano, and L. Pardo. 2012. Membrane protein simulations using AMBER force field and Berger lipid parameters. *J. Chem. Theory Comput.* 8:948–958.

59. Wang, L., R. A. Friesner, and B. J. Berne. 2011. Replica exchange with solute scaling: a more efficient version of replica exchange with solute tempering (REST2). *J. Phys. Chem. B.* 115:9431–9438.

60. Frishman, D., and P. Argos. 1995. Knowledge-based protein secondary structure assignment. *Proteins.* 23:566–579.

61. Schmidt, T. H., and C. Kandt. 2012. LAMBADA and INFLATEGRO2: efficient membrane alignment and insertion of membrane proteins for molecular dynamics simulations. *J. Chem. Inf. Model.* 52:2657–2669.

62. Bechinger, B., and C. Sizun. 2002. Alignment and structural analysis of membrane polypeptides by $^{15}$N and $^{31}$P solid-state NMR spectroscopy. *Conc. Magn. Res. A.* 18:130–145.

63. Aisenbrey, C., and B. Bechinger. 2004. Tilt and rotational pitch angle of membrane-inserted polypeptides from combined $^{15}$N and $^{2}$H solid-state NMR spectroscopy. *Biochemistry.* 43:10502–10512.

64. Salnikov, E., P. Bertani, …, B. Bechinger. 2009. Analysis of the amide $^{15}$N chemical shift tensor of the C($\alpha$) tetrasubstituted constituent of membrane-active peptaibols, the $\alpha$-aminoisobutyric acid residue, compared to those of di- and tri-substituted proteinogenic amino acid residues. *J. Biomol. NMR.* 45:373–387.

65. Bechinger, B., J. M. Resende, and C. Aisenbrey. 2011. The structural and topological analysis of membrane-associated polypeptides by oriented solid-state NMR spectroscopy: established concepts and novel developments. *Biophys. Chem.* 153:115–125.

66. Ulmschneider, J. P., J. C. Smith, …, E. Strandberg. 2012. Reorientation and dimerization of the membrane-bound antimicrobial peptide PGLa from microsecond all-atom MD simulations. *Biophys. J.* 103:472–482.

67. Krivov, G. G., M. V. Shapovalov, and R. L. Dunbrack, Jr. 2009. Improved prediction of protein side-chain conformations with SCWRL4. *Proteins.* 77:778–795.

68. Butterfield, S. M., and H. A. Lashuel. 2010. Amyloidogenic protein-membrane interactions: mechanistic insight from model systems. *Angew. Chem. Int. Ed. Engl.* 49:5628–5654.

69. Cornett, J., F. Cao, …, X.-J. Li. 2005. Polyglutamine expansion of huntingtin impairs its nuclear export. *Nat. Genet.* 37:198–204.

70. Allen, W. J., J. A. Lemkul, and D. R. Bevan. 2009. GRIDMAT-MD: a grid-based membrane analysis tool for use with molecular dynamics. *J. Comput. Chem.* 30:1952–1958.

71. Mori, T., F. Ogushi, and Y. Sugita. 2012. Analysis of lipid surface area in protein-membrane systems combining Voronoi tessellation and Monte Carlo integration methods. *J. Comput. Chem.* 33:286–293.

72. Burke, K. A., E. A. Yates, and J. Legleiter. 2013. Amyloid-forming proteins alter the local mechanical properties of lipid membranes. *Biochemistry.* 52:808–817.

73. Huang, H. W. 1995. Elasticity of lipid bilayer interacting with amphiphilic helical peptides. *J. Phys. II France.* 5:1427–1431.

74. Zemel, A., A. Ben-Shaul, and S. May. 2004. Membrane perturbation induced by interfacially adsorbed peptides. *Biophys. J.* 86:3607–3619.

75. Zemel, A., A. Ben-Shaul, and S. May. 2005. Perturbation of a lipid membrane by amphipathic peptides and its role in pore formation. *Eur. Biophys. J.* 34:230–242.

76. Wimley, W. C. 2010. Energetics of peptide and protein binding to lipid membranes. *Proteins.* 13:14–23.

77. Lashuel, H. A., and P. T. J. Lansbury, Jr. 2006. Are amyloid diseases caused by protein aggregates that mimic bacterial pore-forming toxins? *Q. Rev. Biophys.* 39:167–201.

78. Zhang, M., J. Zhao, and J. Zheng. 2014. Molecular understanding of a potential functional link between antimicrobial and amyloid peptides. *Soft Matter.* 10:7425–7451.

79. Monoi, H., S. Futaki, …, K. Yoshihara. 2000. Poly-L-glutamine forms cation channels: relevance to the pathogenesis of the polyglutamine diseases. *Biophys. J.* 78:2892–2899.

80. Hirakura, Y., R. Azimov, …, B. L. Kagan. 2000. Polyglutamine-induced ion channels: a possible mechanism for the neurotoxicity of Huntington and other CAG repeat diseases. *J. Neurosci. Res.* 60: 490–494.

81. Kagan, B. L., Y. Hirakura, …, R. Azimova. 2001. The channel hypothesis of Huntington's disease. *Brain Res. Bull.* 56:281–284.

82. Bechinger, B. 2009. Rationalizing the membrane interactions of actinic amphipathic antimicrobial peptides by their molecular shape. *Curr. Opin. Colloid Interface Sci.* 14:349–355.

83. Bechinger, B., and C. Aisenbrey. 2012. The polymorphic nature of membrane-active peptides from biophysical and structural investigations. *Curr. Protein Pept. Sci.* 13:602–610.